A&A, 706, A358 (2026)
https://doi.org/10.1051/0004-6361/202557566

Astronomy & Astrophysics

Measurement of the extragalactic background light at 8600 Å using dark cloud shadow and the Ca II-triplet lines⋆

L. K. Haikala[1,⋆⋆], K. Mattila[2,⋆⋆], and P. Väisänen[3,4]

[1] Instituto de Astronomia y Ciencias Planetarias, Universidad de Atacama, Copayapu 485, Copiapo, Chile
[2] Department of Physics, University of Helsinki, Gustaf Hällströminkatu 2, FI-00014 Helsinki, Finland
[3] Finnish Centre for Astronomy with ESO, FINCA, FI-20014 University of Turku, Turku, Finland
[4] South African Astronomical Observatory, P.O. Box 9, Observatory, 7935 Cape Town, South Africa

Received 6 October 2025 / Accepted 25 December 2025

ABSTRACT

We present the results of a measurement of the near-infrared extragalactic background light (EBL). The surface brightness towards the opaque intermediate-latitude globule DC303.8-14.2 was obtained using ESO VLT/FORS spectrophotometry. Long-slit spectra covering the opaque core and the almost unobscured area north of the cloud were measured using the nodding-along-the-slit measuring technique, thus providing a differential spectrum opaque core – transparent area. It is free of most of the foreground components, also excluding most of the airglow time variations. The scattered integrated starlight (ISL) from the dark core itself is the only remaining major foreground component when extracting the EBL from the differential spectrum. The scattered starlight spectrum in the wavelength domain 8450–8700 Å is dominated by the strong Ca II triplet Fraunhofer lines at λ 8498, 8542, 8664 Å, whereas the integrated light of galaxies and other contributors to the EBL intensity produce a smooth spectrum without these lines. We used the GAIA RVS spectral database to construct a template for the scattered ISL spectrum; another template was obtained by using the globule's semi-transparent bright rim. The resulting EBL intensity as derived from the λ 8542 Å line is $I_{\rm EBL} = 1.62 \pm 0.76(\sigma_{\rm stat})\ 10^{-9}$ erg cm^{-2} s^{-1} Å^{-1} sterad^{-1} or $13.8 \pm 6.5(\sigma_{\rm stat})$ nW m^{-2} sr^{-1}; this represents a tentative detection at 2.1σ level; the scaling uncertainty is ±10%.

Key words. methods: observational – techniques: spectroscopic – dust, extinction – solar neighborhood – Galaxy: stellar content – diffuse radiation – diffuse radiation

1. Introduction

The UV/optical/near-IR extragalactic background light (EBL) contains a large fraction of the energy released in the Universe since the re-ionisation epoch. The importance of the EBL is emphasised by the detection of the cosmic far-infrared background, the dust-processed fraction of the EBL (Hauser et al. 1998). EBL puts important constraints on the formation and early evolution of galaxies and the star formation history of the Universe. The integrated galaxy light (IGL) puts a firm lower limit to the EBL and it has been determined with increasing accuracy in the last ten years by Driver et al. (2016), Koushan et al. (2021) and Tompkins et al. (2026); the extrapolated part beyond the current $m_{\rm lim} \sim 30$ mag may still remain somewhat uncertain. Reaching beyond the magnitude limit of the IGL, the EBL represents an inventory of all the light, especially the diffuse light, produced by nucleosynthesis in stars outside the galaxies plus accretion into active galactic nuclei (AGN). Low surface brightness galaxies and individual intergalactic or interhalo stars are possible contributors to the EBL. Moreover, the hypothetical decaying of elementary particles in a suitable energy range has been discussed in the past.

The measurement of the optical EBL has turned out to be a tedious problem because the foreground components, the zodiacal light (ZL) and airglow (AGL), are much brighter than the EBL. We have recently (Mattila et al. 2017b) achieved a measurement of the EBL at 400 nm, utilising the shadowing effect of a dark nebula on the background light. A differential measurement of the surface brightness of a high-latitude dark nebula and its surrounding area, which is (almost) free of obscuring and scattering dust, provides a signal that is free of ZL and AGL and is due to two components only: (1) the EBL and (2) the integrated starlight (ISL) diffusely scattered from interstellar dust in the cloud and, to smaller degree, from its surroundings.

The key issue of the dark cloud method is using the characteristic absorption line spectrum of the scattered light which, for the line depths, is a copy of the ISL spectrum. The EBL and ISL have different spectra: the ISL spectrum has the characteristic Fraunhofer lines and discontinuities (such as the Balmer and 400 nm jumps), while the EBL spectrum is smooth; summing up radiation over a large redshift range washes out the spectral features. The transmitted EBL signal is present in the transparent OFF area only. It has the effect that in the *on–off* spectrum (opaque core minus transparent area) the Fraunhofer line depths, measured in units of the adjacent continuum level of the spectrum, are larger than they are in the pure scattered ISL spectrum (see Fig. 1).

The tentative EBL detection at 400 nm (Mattila et al. 2017b) has suggested that there remains space for an unknown EBL component of approximately equal magnitude to the

⋆ Based on observations done at the European Southern Observatory, La Silla Paranal Observatory, Chile (programs 099.A-0028, 0102.A-0280 and 0104.A-0192).

⋆⋆ Corresponding authors: lauri.haikala@uda.cl; kalevi.mattila@helsinki.fi

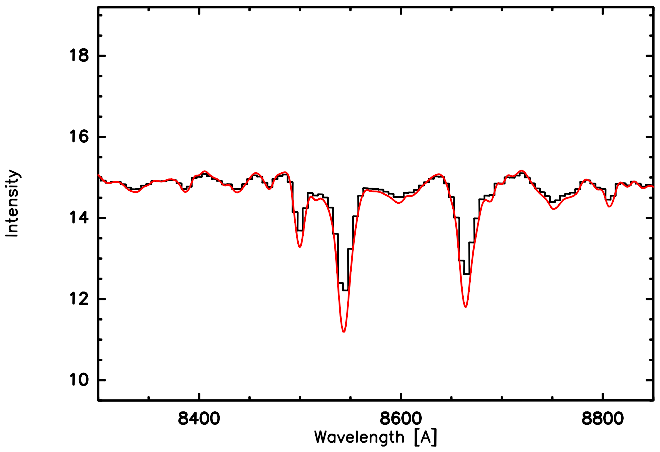

Fig. 1. Model for the Ca II triplet lines in the synthetic scattered integrated starlight (ISL) spectrum (black line) for an assumed continuum intensity of 15 units and a spectral resolution of 10 Å; the Pickles spectrum library has been adopted (Lehtinen & Mattila 2013). The red line shows the *on–off* spectrum (opaque dark core minus transparent background sky) in the presence of an EBL of 5 units.

well-established IGL. An excess EBL component at 0.8−1.6 μm, approximately equal to the IGL, has been announced by Matsuura et al. (2017). More recently, Zemcov et al. (2017), Lauer et al. (2021, 2022), Symons et al. (2023), and Postman et al. (2024), using the *New-Horizons*-LORRI broadband imager 440–870 nm, have found different EBL values, varying from approximately two times the IGL down to no excess above the IGL level.

In order to further constrain this unknown EBL component and also to provide independent support for EBL detections, ours and the others, we need a spectral coverage that is as wide as possible. Because of the continuum and cumulative Lyman line absorption by integalactic HI clouds, the EBL at 400 nm measures the EBL only up to the redshift of $z \sim 3$. At 860 nm, the range is strongly expanded, up to $z \sim 7.5$. The aim of the present study is to apply the dark cloud shadow method to longer wavelengths.

The strong Ca II triplet λ 8498/8542/8662 offers the best possibility in the red–near-IR wavelength range 550–1000 nm. Along a similar line of thought, Korngut et al. (2022) have used the Ca II triplet line 8542 Å to measure the absolute intensity of the ZL, a serious foreground hindrance for the measurement of the EBL.

The high latitude globule DC303.8-14.2 (Hartley et al. 1986), first listed as Sandqvist 160 (Sandqvist 1977), located at $\alpha = 13{:}07{:}40.0$, $\delta = -77{:}00{:}00$ (J2000), is a suitable target for the application of the dark cloud method. It has a large core depth, $\tau(860\,\mathrm{nm}) \geq 10$, and OFF areas with sufficient transparency, $\tau(860\,\mathrm{nm}) \leq 0.5$, are available outside the core (Kainulainen et al. 2007). Low-resolution spectra have already been obtained with NTT+EFOSC by Lehtinen & Mattila (2013).

2. Observations and data reduction

The FORS2 (Appenzeller et al. 1998) DC303.8-14.2 preimaging and the LSS spectroscopic data were acquired in service mode during 2017, 2019, 2020, and 2021 on the VLT UT1 telescope Antu. The instrumental set-up of the spectroscopy is listed in Table 1. Due to the faintness of the EBL signal and the brightness of the expected sky background, dark time and photometric sky conditions were requested. Because of the southern declination of the target (–77 deg), the observations were limited to time slots of $\lesssim$6 h. Standard stars were observed during the observations to calibrate the spectrometer response.

2.1. The observation strategy

DC303.8-14.2 and the background to the north was pre-imaged with FORS2 (I_BESS filter) in order to find an optimal position for the longslit, i.e. avoiding stars as much as possible (see Fig. 2). Due to the strong and variable airglow spectral lines in the 800–900 nm, region and high background sky brightness of $\gtrsim$200–300 10^{-9} erg cm^{-2} s^{-1} Å^{-1} sterad^{-1} (hereafter cgs-unit) the measurement of the expected I_{EBL} signal of 1–5 cgs-units is technically very demanding; for example, it requires an exceptionally good flat-fielding accuracy of ~0.2%, when applying the simple slit technique. However, such high accuracy cannot be reached with standard flat-field procedures. Therefore, instead of a simple single long-slit spectrum across the nebula, the following more sophisticated strategy was used. The core of the globule and the adjacent transparent comparison areas were observed using the same part of the slit (and exactly the same detector pixels). This was achieved by nodding the telescope relatively rapidly back and forth by 300″ along the 6.′8 (408″) long slit so that the slit positions overlapped by 100″ during individual nods (Fig. 2). The night-sky brightness at 850–864 nm is dominated by airglow which varies on timescales of minutes. An *on–off* cycle time of 5 minutes can be done with 90 seconds *on*, 90 seconds *off*, when nodding is done along the slit (ESO observing template FORS2-lss_obs_off_fast). The DC303.8-14.2 spectroscopy data were collected during 27 observing blocks of 11 nods each. The number of observations in each year and month are listed in Table A.1.

2.2. Data reduction

The ESO esoreflex-2.9.1 pipeline and the ESO Common Pipeline library, EsoRex, were used to reduce individual spectra. The pipeline was used to analyse the standard star measurements and to produce the FORS2 efficiency and response tables during the observing runs. EsoRex fors_calib was used to rectify and wavelength calibrate the spectra and to produce the MASTER_BIAS, the MASTER_NORM_FLAT_LSS images, and the GLOBAL_DISTORTION_TABLE. Flat-fielding must be applied if the *on–off* position continuum level difference is not zero even if the same detector pixels are used. The MASTER_NORM_FLAT_LSS was smoothed to remove the high frequency noise, but conserving the flat-field large-scale gradients. The target spectra were first bias subtracted, then flat-fielded using the smoothed MASTER_NORM_FLAT_LSS and remapped using EsoRex fors_science, but not flux calibrated

The MAPPED_ALL_SCI_LSS spectra provided by fors_science were collected for each observing block. These spectra still have the strong sky airglow lines. The sky subtraction was done by subtracting the average of the two *off* spectra taken at 300″ north, one immediately before and one after the *on* spectrum. This was done separately for FORS2 detectors, Chip1 (A), and Chip2 (B). Thus, each of the 27 observing blocks of 11 telescope nods provided ten *on–off* spectra for the two detector chips. The Chip2 *on–off* spectra provide the difference between the globule core and bright rim areas and the middle *off* area positions, while the Chip1 *on–off* spectra provide the difference between the middle *off* area and the northernmost *off* area positions (for the location of the areas, see Fig. 2). After the *on–off* subtraction the flat-fielding affects only the

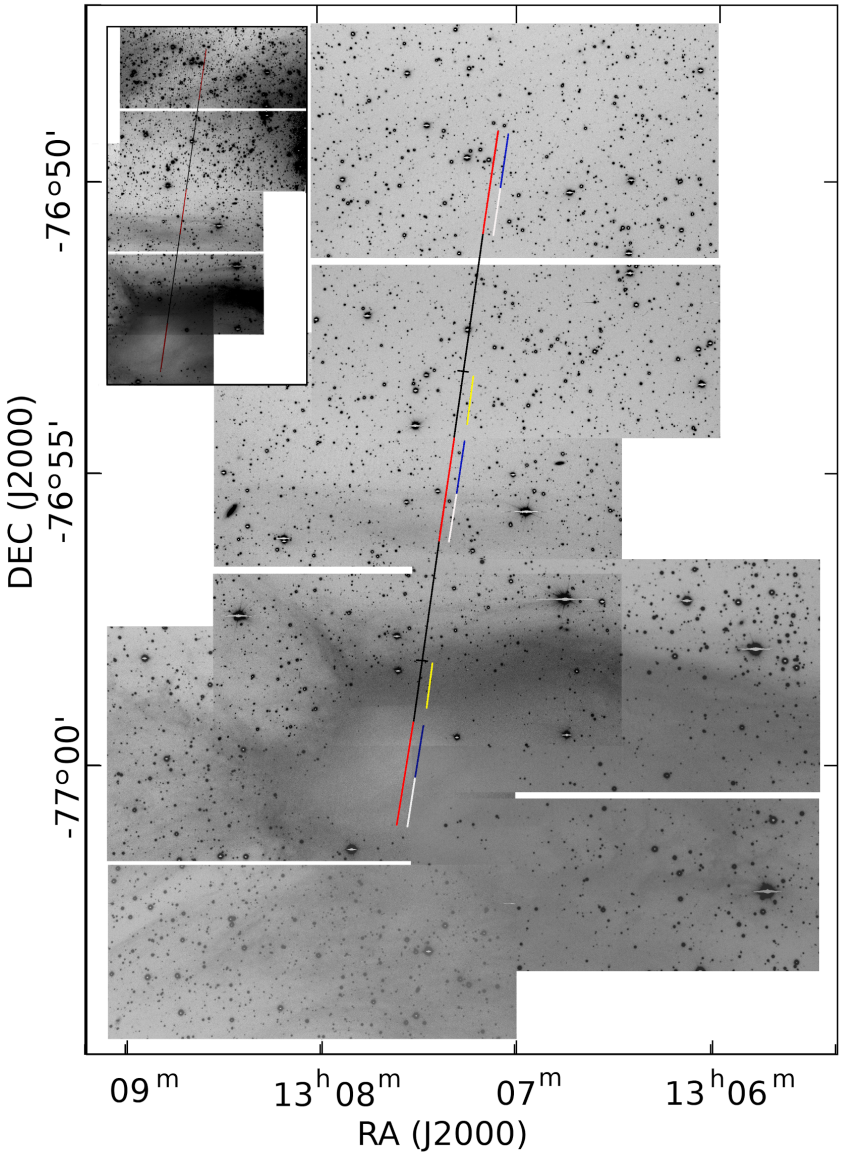

Fig. 2. Mosaic of the I–BESS images observed during the DC303.8 pre-imaging. The position of the two overlapping FORS longslit positions on the sky during the nodding are superposed on the image. The overlapping 100″ sections are indicated in red. The southernmost red section covering the globule core marks the position of the southern 100″ of the FORS2 CHIP2 during the first nod integration. The northernmost red section marks the northern 100″ part of CHIP1 during the second nod integration. The centermost red section is covered first by CHIP1 during the first nod integration and by the CHIP2 100″ section during the second nod integration. The slit sections discussed in the text are indicated in white, blue, and yellow.

difference spectrum as the bulk of the atmospheric continuum and AGL intensities cancel out. The *on–off* spectra from the 27 observing blocks were first cropped so that the pixels in the spectra aligned correctly and then collected to a single database. The final database contained 270 reduced *on–off* spectra for CHIP1 and CHIP2 each.

The ADU difference spectra were corrected for aperture efficiency and flux calibrated using the spectral response tables from standard star measurement nearest in time. These spectra, now in units of erg cm^{-2} s^{-1} Å^{-1} per readout pixel (binned by 2), were then converted to surface brightnesses. The solid angle of a pixel is given by slit width (2.5″) × pixel size (0.″25) = 1.469 10^{-11} sterad.

The 270 *on–off* spectra were median averaged for the A and B detectors. Using the median rather than the average helped to eliminate extreme AGL time variability outliers and cosmic-ray hits. The resulting averaged 2D spectra contain numerous stars, most of which are not visible in the original single *on–off* spectra. Because of the high extinction in the direction of DC303.8-14.2 the number of visible stars in the B detector averaged spectra is lower than that in the OFF region covered by detector A. The stars and the remaining instrumental artefacts were cleaned from the averaged spectra. Finally 1D spectra covering the slit sections discussed in the text (see Table 2 and Fig. 2) were formed by averaging the 2D median averaged spectra in the slit direction using the IRAF routine blkavg. The average was adopted because the time-variability aspect does not occur in the median averaged 2D spectra and because of the somewhat smaller rms compared to the median. In the used instrumental set-up, the FORS spectral resolution is 9.0 Å, but the readout dispersion (after binning by two) is 0.84 Å. Thus, the 1D spectrum was block averaged by four pixels in the dispersion direction. The resulting surface brightnesses of the Core-up and Bright_rim sections were then ∼19 and ∼37 cgs-units, respectively. These values are in reasonably good agreement with the surface brightnesses observed with EMMI at the New Technology Telescope at La Silla (Lehtinen & Mattila 2013).

The primary source of noise in the 1D *on–off* spectra is due to atmospheric emission and the airglow lines during nodding. Different from the atmospheric continuum, the emission due to airglow lines varies randomly during the nodding producing 1/f noise. If the variation of the airglow lines is linear

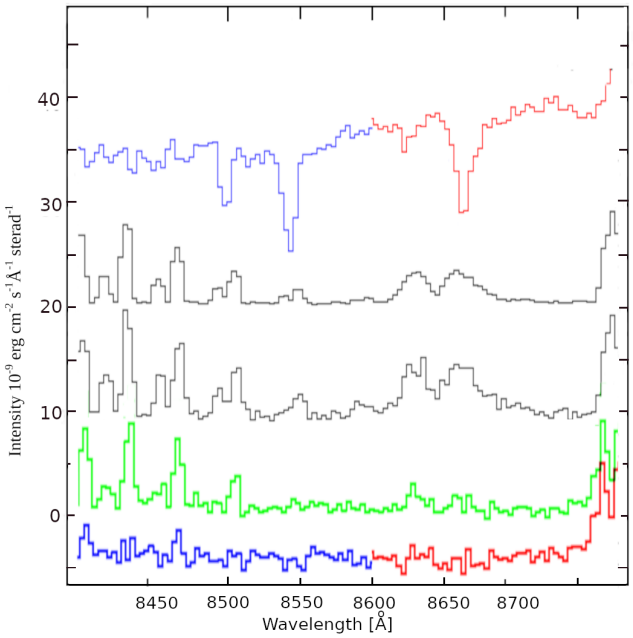

Fig. 3. From top to bottom: Chip 2 extracted Bright_rim spectrum combined from 179 *on–off* spectra below 8600 Å (in blue) and 228 *on–off* spectra above 8600 Å (in red). A typical airglow spectrum scaled by 1/500 and shifted upwards by 20 cgs-units. The standard deviation of the intensities along the slit in the Chip 2 Bright_rim 2D spectrum shifted upwards by 4 cgs-units. The A_100″-off spectrum (green) from the sum of all 270 *off–on–off* spectra; it has been shifted upwards by 3 cgs-units. The A_100″-off spectra for the sub-sets of 179 and 228 individual spectra, selected for minimum-AGL residuals in blue and red for $\lambda < 8600$ Å and $\lambda > 8600$ Å, respectively.

in time, using the average of the two off spectra taken immediately before and after the on spectrum as the off spectrum helps to suppress the airglow noise in the *on–off* spectrum. The Ca II triplet lines coincide in wavelength with strong airglow lines, the 8498 Å and 8542 Å lines (hereafter lines 1 and 2, respectively) with the hydroxyl (OH) molecule ro-vibrational 6–2 transition lines, and the 8662 Å line (hereafter line 3) with broad O2 (1–0) lines. The intensity of residuals due to the O2 line were generally lower than those of the OH lines; in addition, the OH and O2 airglow line residuals varied at times in opposite directions.

A visual selection of the least contaminated *on–off* spectra was made separately for the wavelength ranges 8500–8600 Å and 8600–8700 Å, which overlap lines 1 + 2 and line 3, respectively. The first sub-set contains 179 and the second contains 228 spectra. The relation between the airglow lines and the noise in the summed spectra is demonstrated in Fig. 3. Although the strengths of the AGL bands in the *on–off* spectra have been reduced (by a factor of $\sim 10^{-2}$) compared to their total sky levels, the spectra are still contaminated by the AGL residuals at a low level. Elimination of the spectra most strongly affected by airglow variations strongly suppresses the AGL residual noise in the low extinction Chip 1 summed up A_100″-off position where no Ca II triplet lines are expected (Fig. 3). All the final spectra in the slit sections discussed in this paper are shown in Fig. A.2.

3. Separation of the EBL and the scattered light

The dust in DC303-14.2 acts as an obscuring screen in front of the extragalactic background light. The attenuation of the

Table 1. The FORS2 instrumental set-up.

Telescope/Instrument	VLT-UT1/FORS2
mode	LSS
Grism	GRIS_1028z
Filter	OG590
Spectral resolution	9.0 ÅFWHM
Detector	2× MIT
Size	2× (2048 × 1024)[a]
LSS slit width	2.″5
LSS slit length	6.′8
LSS position angle	8°
Spatial scale	0.″25/pixel[a]
Dispersion	0.84 Å/pixel[a]
Wavelength range	7900 Å–9500 Å

Notes. [(a)] After binning the CCDs by 2 × 2.

Table 2. Names used for the *on-off* spectra taken along the long-slit shown in Fig. 2 and their extensions.

Name	Pos. *on*[a]	Pos. *off*[a]	Colour in Fig. 2	Cleaned[a] width[b]
Core-100″	0″–100″	300″–400″	Red	86″
Core-low	0″–50″	300″–350″	White	46″
Core-up	50″–100″	350″–400″	Blue	40″
Bright_rim	115″–161″	415″–461″	Yellow	38″
A_100″-off	300″–400″	600″–700″	Red	64″
A_low-off	300″–350″	600″–650″	White	31″
A_core-off	350″–400″	650″–700″	Blue	33″

Notes. [(a)] The *on* and *off* coordinates are counted from the southern end of the CHIP2 slit covering the globule core. [(b)] Slit section width after cleaning stars.

EBL depends on the line-of-sight extinction: blocking is strong towards the opaque core, while less shadowing occurs in the transparent outer areas. The scattered starlight dominates over the effects of the EBL in the observed *on–off* surface brightness difference. The situation in the optical differs from that with the X-ray shadows seen towards dark clouds and globules (see e.g. Freyberg et al. 2004; Yeung et al. 2023) where the attenuation is caused by pure absorption of cold gas in the cloud.

In order to disentangle the EBL and the scattered starlight components one can make use of spectroscopic observations in suitable wavelength slots where the scattered starlight has strong spectral features, absorption lines or discontinuities. For the present study we used the Ca II absorption line triplet at λ8499/8542/8662. It is one of the strongest spectral features in the red/near-IR integrated starlight, and is therefore well suited also for the study of low surface brightness targets. The triplet is prominently present in our scattered light spectra of DC303.8-14.2.

3.1. The components of the observed on–off spectrum

The observed *on–off* surface brightness difference, $\Delta I_{\rm obs}(\lambda)$, has two components: the scattered starlight, $I_{\rm sca}(\lambda)$, and the extragalactic background light, $I_{\rm EBL}$. The observed difference can be

expressed as

$$\Delta I_{\rm obs}(\lambda) = I^{\rm on}_{\rm sca}(\lambda) - I^{\rm off}_{\rm sca}(\lambda) + I_{\rm EBL}(e^{-\tau} + f_{\rm sca}(\tau)) - I_{\rm EBL} = \Delta I_{\rm sca}(\lambda) - I_{\rm EBL} h(\tau), \quad (1)$$

where $I^{\rm on}_{\rm sca}(\lambda)$ and $I^{\rm off}_{\rm sca}(\lambda)$ are respectively the intensities of starlight as scattered by dust in the cloud and in the semi-transparent *off* area; the term $I_{\rm EBL}e^{-\tau}$ stands for the transmitted EBL; and $I_{\rm EBL}$ is assumed to be constant over the wavelength range relevant in this study $\lambda = 8450 - 8700$ Å.

Not only the starlight, but also the photons of the isotropic EBL are scattered by the dust; this scattered EBL component is given by the term $I_{\rm EBL}f_{\rm sca}(\tau)$. Here, we introduce the notation $h(\tau) = 1 - e^{-\tau} - f_{\rm sca}(\tau)$, which we call the attenuation factor. It gives the fraction by which the EBL is attenuated in the direction of the cloud relative to a transparent *off* area: $h(\tau) = 1$ for the case of complete obscuration and $h(\tau) = 0$ for no obscuration. For small and moderate optical depths, $\tau \lesssim 1{-}2$, scattering compensates much of the cloud's obscuring effect. Even for high opacities it still amounts to a substantial fraction of $I_{\rm EBL}$. For the high-opacity core area of DC303-14.2, the scattered light seen towards the core is dominated by the outer layers up to $\tau \approx 2{-}3$ mag, whereas the core itself dominates the attenuation term $e^{-\tau}$.

Values of $f_{\rm sca}(\tau)$ for different cloud opacities and dust scattering properties have been calculated using Monte Carlo radiative transfer modelling (Mattila 1976). However, such results depend strongly on the adopted dust-scattering parameters. Therefore, we have estimated the $f_{\rm sca}(\tau)$ values empirically, by using the scattered starlight values, $I_{\rm sca}(\lambda)$, for the Core-100″ and the Bright_rim of DC303.8-14.2 as a guide. Based on these estimates we have derived for the Core-100″ and Bright_rim areas the values $h(\tau) = 0.92$ and 0.69, respectively. Their systematic errors were estimated to be 2% and 4%, respectively. For details we refer to Appendix C.

3.2. Model fitting of the opaque core spectrum

The observed spectrum $\Delta I_{\rm obs}(\lambda)$ is fitted in accordance with Eq. (1). The spectrum of the scattered starlight from the cloud can be represented as the product of two factors,

$$I^{\rm on}_{\rm sca}(\lambda) = i_{\rm ISL}(\lambda) G^{\rm on}_{\rm sca}(\lambda), \quad (2)$$

where $i_{\rm ISL}(\lambda)$ stands for the normalised spectrum of the impinging integrated starlight. It is normalised to 1 at a reference wavelength λ_0:

$$i_{\rm ISL}(\lambda) = I_{\rm ISL}(\lambda)/I_{\rm ISL}(\lambda_0). \quad (3)$$

Here $G^{\rm on}_{\rm sca}(\lambda)$ accounts for the intensity and gradient (reddening or bluing) of the scattered light relative to the starlight spectrum, $i_{\rm ISL}(\lambda)$, as caused by the wavelength-dependent scattering and extinction in the cloud. $G^{\rm on}_{\rm sca}(\lambda)$, is assumed to be, over a limited wavelength range, linear function of λ.

$$G^{\rm on}_{\rm sca}(\lambda) = G^{\rm on}_{\rm sca}(\lambda_0)[1 + grad^{\rm on} \times (\lambda - \lambda_0) \quad (4)$$

We write in a similar way for the *off* position,

$$G^{\rm off}_{\rm sca}(\lambda) = G^{\rm off}_{\rm sca}(\lambda_0)[1 + grad^{\rm off} \times (\lambda - \lambda_0) \quad (5)$$

and for the difference *on–off*

$$\Delta G^{\rm on-off}_{\rm sca}(\lambda) = \Delta G^{\rm on-off}_{\rm sca}(\lambda_0)[1 + grad(\lambda - \lambda_0) \quad (6)$$

where $grad = grad^{\rm on-off}$.

For the fitting of the observed *on–off* surface brightness difference, $\Delta I_{\rm obs}(\lambda)$, as given by Eq. (1), we have used the IDL programme `MPFITFUN`[1]. For the fitting it is represented as

$$\Delta I_{\rm obs}(\lambda) = [p_0 + p_1(\lambda - \lambda_0)] i_{\rm ISL}(\lambda) - h(\tau) I_{\rm EBL}. \quad (7)$$

Here the parameters p_0 and p_1 correspond to $G_{\rm sca}(\lambda_0)$ and *grad*. For λ_0 we adopt 860.0 nm.

For the estimation of $I_{\rm EBL}$ we adopted two different approaches: First, we constructed the integrated starlight spectrum $i_{\rm ISL}(\lambda)$ by adding up a large number of stellar RVS spectra as provided in the GAIA3 Data release (see Section 3.2.1).

Secondly, we utilised the observed spectrum of the bright rim. Because of the different values of the attenuation factor $h(\tau)$, the core and the rim spectra are influenced by different amounts of EBL; by combining the two spectra we can determine $I_{\rm EBL}$ without explicitly knowing the integrated starlight spectrum $i_{\rm ISL}(\lambda)$ (see Section 3.2.2).

We note that while the scattered light has a continuum gradient (reddening or bluing), which differs from the impinging ISL spectrum, the depths, and profiles of the Fraunhofer lines, including the Ca II triplet, remain unchanged.

3.2.1. Model fit using GAIA RVS integrated starlight spectrum

The interstellar radiation field (ISRF) in the optical and near-infrared is mainly produced by the integrated starlight (ISL), the sum of light from individual stars distributed over all directions and magnitudes. A modest (10–20%) indirect contribution is added by the diffuse galactic light (DGL), that is starlight scattered off interstellar dust. The absorption line spectrum of the DGL is the same as that in the ISL.

The recent Gaia Data Release 3 has made available the Radial Velocity Spectrometer (RVS) mean spectra for ∼1 million stars brighter than $G_{\rm RVS} \sim 14$ mag ($G \sim 15$ mag), distributed all over the sky. We have derived the integrated starlight spectrum for a number of selected areas by adding up the contributions of all stars with $G_{\rm RVS} \leq 12$ mag, which is the limit of completeness for the mean RVS spectra in Gaia DR3.

Circular areas were selected with diameters 8°–20°, depending on the star density in the area. In view of the position of our target globule at $l = 303.^{\circ}8, b = -14.^{\circ}2$, areas were chosen at latitudes $0, \pm10, -15, \pm30, \pm60°$ for each of the longitudes 240, 270, 300, 330, 360°, plus the polar caps, $b = \pm90°$. The number of stars was mostly 4000–5000 per area. The selection of these GAIA RVS areas was done with the scattering properties of the interstellar dust in mind.

Observations of the DGL and scattered light in dark nebulae have shown that the scattering function $S(\Theta)$ is strongly forward-throwing. It is frequently approximated by the analytic expression according to Henyey & Greenstein (1941), characterised by the asymmetry parameter $g = \langle \cos\Theta \rangle$. Observations have indicated that $g \approx 0.6{-}0.9$ (see review by Gordon 2004). Specifically for globules and dense cloud cores the observational results have been more restrictive, however. The asymmetry parameter values for them at optical to near-IR wavelengths range between $g = 0.7$ and 0.9 (Mattila 1970; Witt & Stephens 1974; Fitzgerald et al. 1976; Witt et al. 1990; Togi et al. 2017; Mattila et al. 2018). We adopt for our estimates for DC303.8-14.2 the value $g = 0.75$. In order to test the effect of a less forward-throwing scattering func-

[1] https://cow.physics.wisc.edu/~craigm/idl/mpfittut.html

tion we have also calculated the integrated starlight spectrum for another, albeit unrealistic, case of $g = 0.5$.

For $g = 0.75$ the illumination of the globule comes from a relatively narrow cone: 65% comes from $\Theta < 30°$ and 77% from $\Theta < 40°$. The distribution of our selected sky areas, as listed above, covers this range well. We divided the sky between $240° < l < 360°$ and $-90° < b < 90°$ into 42 'parcels', each one with a GAIA RVS area in its centre. For each GAIA RVS area the fluxes, $j_k^i(\lambda)$, of all GAIA RVS stars with $G_{\rm RVS} \leq 12$ mag were added up, and the sum was normalised to 1 at $\lambda_0 = 860$ nm. It is denoted by $\sum_i j_k^i(\lambda)$. This normalised sum spectrum represents the spectrum of the whole parcel. To each parcel, k = 1.42 a weight was assigned according to

$$W_k = A_k \times \bar{I}_k^{\rm ISL} \times S_k^{\rm H-G}(\Theta_k) \tag{8}$$

where A_k is the area and $\bar{I}_k^{\rm ISL}$ the mean ISL surface brightness of the parcel; $S_k^{\rm H-G}(\Theta_k)$ is the intensity of the scattered light according to the Henyey–Greenstein scattering function for $g = 0.75$. The scattering angle Θ_k is the angle between the directions towards parcel k and the globule; $\bar{I}_k^{\rm ISL}$ was taken from the Pioneer 10/11 R band starlight mapping (see Gordon et al. 1998) and the web page[2].

$$\sum_{k=1}^{42} W_k \times \Sigma_i j_k^i(\lambda). \tag{9}$$

The weighted sum spectrum, normalised to 1 at $\lambda_0 = 860$ nm, was convolved with the FORS instrumental profile and resampled then to the same channel width as the observed FORS spectra (see Appendix B). This spectrum was used as the ISL spectrum $i_{\rm ISL}(\lambda)$ in Eqs. (2) and (3).

Results for the Bright_rim and Core-up spectra, fitted according to Eq. (7) with the GAIA RVS spectrum for $g = 0.75$, are shown in Figs. 4 and 5. In the lower part of Fig. B.1 we compare the GAIA interstellar radiation field spectra for the two cases $g = 0.75$ and $g = 0.50$. The depths of the three Ca II lines for $g = 0.50$ differ by no more than 0.5% from the case $g = 0.75$. It can be concluded that that even for the extreme g-value of 0.5 the difference in the GAIA-based radiation fields for $g = 0.50$ and $g = 0.75$ would be much smaller than the observational uncertainties of the line depths (see Fig. 4). We conclude that the uncertainty caused by the adopted g-value can be neglected.

Because a substantial fraction of the ISL comes from stars with $G_{\rm RVS} > 12$ mag, we have to address the question of how much light is missing in our ISL spectra, and whether the RVS spectrum of the stars with $G_{\rm RVS} > 12$ mag differs from that of the brighter ones with $G_{\rm RVS} < 12$ mag.

We performed the star counts using the GAIA DR3 red magnitudes $G_{\rm RP}$. The magnitude range covered was 2–20 mag The three areas chosen for the counts, $(l, b) = (300,–5)$, (300,–15), and (300,–30), covered the sky area most relevant for illumination of the globule. The fraction of the ISL contributed by stars with $G_{\rm RP} > 12$ is 48%, 30%, and 23% of the total ISL for these three areas.

Secondly, we constructed a synthetic model for the ISL spectrum. The STELIB library was used for stellar spectra, and a simple Galaxy model was constructed with realistic values for the distribution parameters for stars of different spectral types and luminosity classes. The model and the results for $|b| = 11.5°$ are presented in Appendix E.

In summary, the results of the STELIB model show that the ISL spectrum derived using the GAIA RVS spectra for the magnitude-limited sample, $G_{\rm RVS} \leq 12$ mag, can be considered as a good representation of the total ISL spectrum as well.

3.2.2. Model fit using the bright rim spectrum as template

From Eq. (7), written for the bright rim spectrum, we can solve $i_{\rm ISL}$; we use it to replace $i_{\rm ISL}$ in the expression for the dark core:

$$\Delta I_{\rm obs}^{\rm DC}(\lambda) = \frac{p_0^{\rm DC} + p_1^{\rm DC} \times (\lambda - \lambda_0)}{p_0^{\rm BR} + p_1^{\rm BR} \times (\lambda - \lambda_0)} \Delta I_{\rm obs}^{\rm BR}(\lambda) - \left[h^{\rm DC} - \frac{p_0^{\rm DC} + p_1^{\rm DC} \times (\lambda - \lambda_0)}{p_0^{\rm BR} + p_1^{\rm BR} \times (\lambda - \lambda_0)} h^{\rm BR} \right] \times I_{\rm EBL}. \tag{10}$$

Because the gradient terms $p_1^{\rm DC} \times (\lambda - \lambda_0)$ and $p_1^{\rm BR} \times (\lambda - \lambda_0)$ are much smaller than the terms $p_0^{\rm DC}$ and $p_0^{\rm BR}$, the expression of the dark core spectrum, to be used for the fitting with the bright rim spectrum, can to a good approximation be represented as

$$\Delta I_{\rm obs}^{\rm DC}(\lambda) = \left[\frac{p_0^{\rm DC}}{p_0^{\rm BR}} + q_1 \times (\lambda - \lambda_0) \right] \Delta I^{\rm BR}(\lambda) - \left[h^{\rm DC} - \frac{p_0^{\rm DC}}{p_0^{\rm BR}} h^{\rm BR} \right] I_{\rm EBL}. \tag{11}$$

The term $q_1 \times (\lambda - \lambda_0)$ represents the weak wavelength dependence of the dark core-to-bright rim ratio, as caused by dust extinction and scattering in the globule. For our observed spectra the ratio $p_0^{\rm DC}/p_0^{\rm BR}$ is ≈0.49. With the actual attenuation factors of $h^{\rm DC} \approx 0.92$ and $h^{\rm BR} \approx 0.69$ the resulting effective attenuation factor for the dark-core fitting with the rim fitting becomes $h_{\rm eff} = h^{\rm DC} - (p_0^{\rm DC}/p_0^{\rm BR})h^{\rm BR} = 0.58$. With the absolute errors of ±2% and ±4% for $h^{\rm DC}$ and $h^{\rm BR}$ the absolute (scaling) error for $h_{\rm eff}$ is ±2%.

The GAIA-RVS fitting method (Section 3.2.1) has two advantages regarding the errors. First, the integrated GAIA-RVS spectra have much smaller statistical errors than our FORS bright-rim spectra; second, for the determination of $I_{\rm EBL}$ the larger value of $h(\tau) = 0.92$ as compared to $h_{\rm eff}(\tau) = 0.58$ results in smaller uncertainties for $I_{\rm EBL}$. However, the fitting of the dark core with the bright-rim spectrum is less sensitive to systematic error sources. The simultaneous acquisition of the dark core and bright rim spectra, within the same observing cycle and with identical integration time slots, helps to suppress error sources caused by the different origins of the observed and model spectra in the GAIA-ISL fitting method. The residual errors caused by the airglow time variations are the same in the dark core and bright rim spectra partially cancel out in the fitting method.

4. Results

In order to extract from the observed dark-core spectra measures of the EBL intensity, $I_{\rm EBL}$, we have fitted the Ca II triplet lines in accordance with Eq. (7). We have used two choices for the fitting template: first, the GAIA RVS integrated-starlight spectrum; second, our observed FORS spectrum of the bright rim. We present the results of the fits in Tables 3 and 4, separately for each of the lines, 1, 2, and 3 and also for an overall fit covering the whole wavelength range 8470–8710 Å.

[2] https://www.stsci.edu/~kgordon/pioneer_ipp/Pioneer_10_11_IPP.html

Table 3. EBL values from MPFITFUN fitting utilising the three Ca II triplet lines of the scattered ISL: GAIA spectrum used as template in the fit.

Wavelength	Line(s)	FORS spectrum	rms [cgs]	$h(\tau)I_{\rm EBL} \pm \sigma_{\rm stat}$ [cgs]	$I_{\rm EBL} \pm \sigma_{\rm stat}$[a] [cgs]
8470–8530	line 1	Core-up	0.72	4.69 ± 4.32	
		Core-low	0.62	–2.76 ± 3.73	
		Core-100″	0.52	2.06 ± 3.08	
8515–8590	line 2	Core-up	0.48	0.55 ± 1.29	
		Core-low	0.35	1.95 ± 0.92	
		Mean of Core-up-low		1.48 ± 0.75	1.61 ± 0.82
		Core-100″	0.26	1.50 ± 0.70	1.63 ± 0.76
		Bright_rim	0.62	–0.31 ± 1.69	
8630–8690	line 3	Core-up	0.48	–0.52 ± 1.59	
		Core-low	0.90	4.29 ± 2.95	
		Mean of Core-up-low		0.56 ± 1.39	0.61 ± 1.51
		Core-100″	0.55	1.26 ± 2.16	1.37 ± 2.35
		Bright_rim	0.83	1.43 ± 2.73	
8470–8710	lines 1,2,3	Core-up	0.76	1.93 ± 1.38	
		Core-low	0.76	2.84 ± 1.38	
		Mean of Core-up-low		2.35 ± 0.97	2.55 ± 1.05
		Core-100″	0.59	2.37 ± 1.06	2.58 ± 1.15
		Bright_rim	0.92	1.00 ± 1.67	

Notes. [(a)] For the attenuation factor the value $h(\tau) = 0.92$ was adopted.

Table 4. As Table 3 but using the FORS Bright_rim spectrum as template in the fit.

Wavelength	Line(s)	FORS spectrum	rms [cgs]	$h(\tau)I_{\rm EBL} \pm \sigma_{\rm stat}$ [cgs]	$I_{\rm EBL} \pm \sigma_{\rm stat}$[a] [cgs]
8470–8530	line 1	Core-up	0.76	–0.86 ± 3.54	
		Core-low	0.69	–6.35 ± 3.22	
		Core-100″	0.59	–2.91 ± 2.74	
8515–8590	line 2	Core-up	0.55	0.03 ± 1.46	
		Core-low	0.41	1.56 ± 1.10	
		Mean of Core-up-low		1.02 ± 0.88	1.76 ± 1.52
		Core-100″	0.35	0.99 ± 0.91	1.71 ± 1.57
8630–8690	line 3	Core-up	0.52	–2.24 ± 1.57	
		Core-low	0.90	3.38 ± 2.73	
		Mean of Core-up-low		–0.82 ± 1.37	–1.41 ± 2.36
–		Core-100″	0.55	0.79 ± 1.68	1.36 ± 2.90
8470–8710	lines 1,2,3	Core-up	0.69	0.47 ± 1.15	
		Core-low	0.77	1.36 ± 1.28	
		Mean of Core-up-low		0.87 ± 0.86	1.50 ± 1.48
		Core-100″	0.55	0.87 ± 0.92	1.50 ± 1.59

Notes. [(a)] For the attenuation factor the value $h(\tau) = 0.58$ was adopted.

We consider first line 2 (8542 Å) for which the most conclusive results can be achieved. Results for three different spectral samples, Core-up, Core-low, and Core-100″are given (see Fig. 2 and Table 2 for their positioning along the slit). The spectra Core-up and Core-low provide measures that are independent of each other; the spectrum Core-100″, encompassing them both is seen to be, as expected, closely equal to their mean. This is seen to be true for both fitting methods, that is using either the GAIA RVS starlight sum or the observed Bright_rim spectrum as the template. The two approaches are complementary, each having its advantages and disadvantages. The statistical errors of the GAIA RVS spectrum are clearly much smaller than those for the Bright_rim spectrum. The Bright_rim spectrum is noisier, however, because of its obvious observational errors, a better representative of the total incident radiation field spectrum. Both the dark core and the bright rim are exposed to the same incident radiation field. Because of the different opacities their scattered light continuum spectra may have different slopes, but the depths and shapes of the Ca II triplet lines will remain the same. Combining the results for Core-up, Core-low, and Core-100″, our best estimates for $I_{\rm EBL}$ are $I_{\rm EBL} = 1.62 \pm 0.76$ cgs when using the GAIA template, and $I_{\rm EBL} = 1.74 \pm 1.52$ cgs when using the FORS bright-rim template. They are seen to be in complete agreement with each other, but because they are not independent of each other it is not meaningful to average them. However, their agreement gives support for the validity of each of the two approaches. We adopt the GAIA-fitting value, $I_{\rm EBL} = 1.62 \pm 0.76$ cgs, as our best estimate.

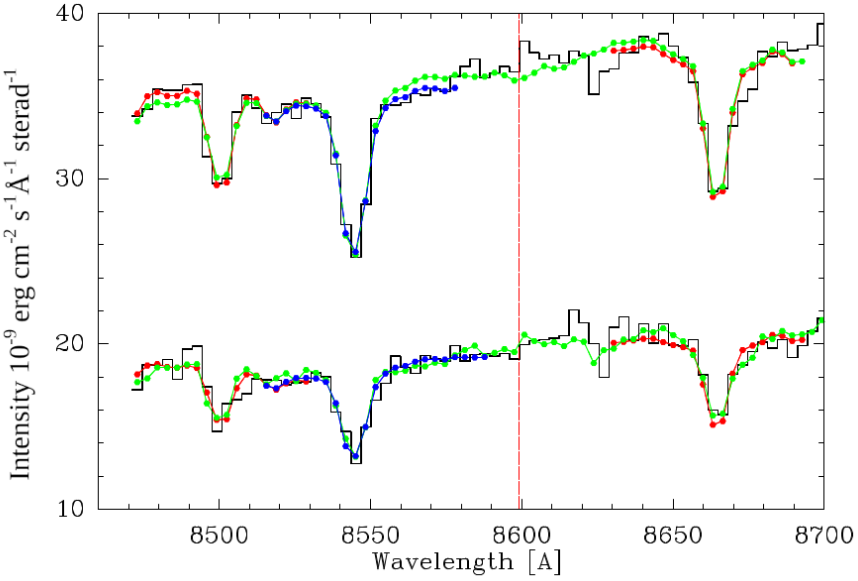

Fig. 4. Bright_rim (upper) and Core-up (bottom) spectra, fitted with the Gaia integrated starlight spectrum. Individual Ca II line fits for lines 1, 2, and 3 are shown in red, blue, and red, respectively; the joint fit of the wavelength range 8470–8700 Å, covering all three lines, is in green.

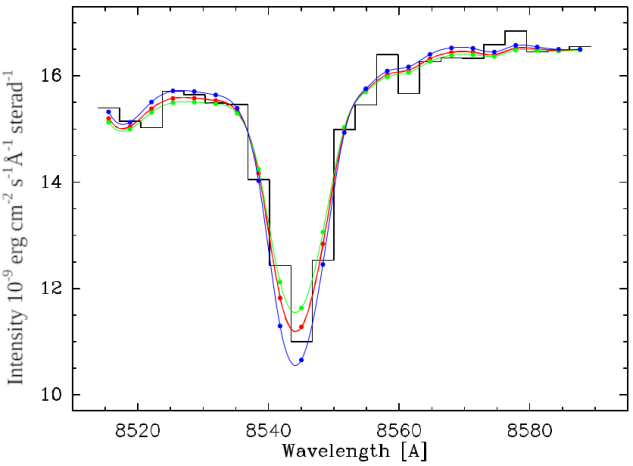

Fig. 5. Line 2 (8542 Å) in the Core_100″ spectrum fitted with the Gaia integrated starlight spectrum. Fits are shown for assumed EBL intensities of $h(\tau)I_{\rm EBL} = 0$, 1.5, and 4.1 10^{-9} erg cm^{-2} s^{-1} Å^{-1} sterad^{-1}, in green, red, and blue, respectively. A cubic spline interpolation was used for plotting the fitted curves.

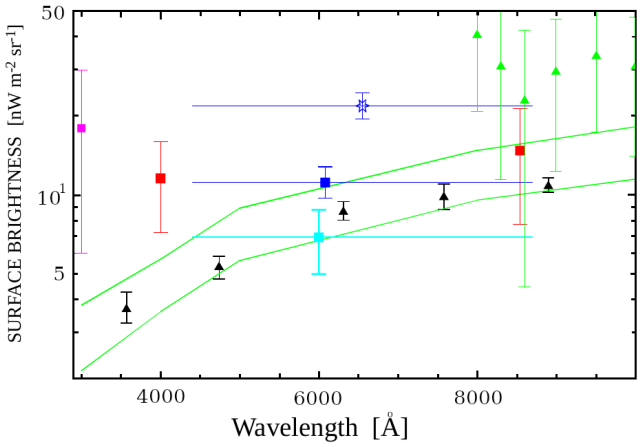

Fig. 6. Some recent results for EBL between 3000 Å and 1.2 μm. Black triangles: Integrated galaxy light (Tompkins et al. 2026). Red squares with 1σ error bars: Photometric EBL measurements at 8542 Å(this paper) and at 4000 Å (Mattila et al. 2017b), green triangles: Matsuura et al. (2017), magenta square: Bernstein (2007), Dark blue square: New Horizons/LORRI measurements (the range of the dark blue bar 4400 – 8700 Å indicates the bandpass of LORRI), blue asterisk: Symons et al. (2023), blue square: Postman et al. (2024), green lines: EBL from γ-ray attenuation, upper and lower limits from Fermi-LAT Large Area Telescope (Fermi-LAT Collaboration 2018), light blue square (the wavelength range was chosen to be the same as the New Horizons/LORRI pass band): Gréaux et al. (2024)

The weakness of line 1 (8498 Å) relative to the noise prevents a useful result from being achieved. In the case of line 3 (8662 Å), the wavelength domain is strongly disturbed, even after the correction described in Section 2.2, by residuals of the broad rapidly variable airglow feature of O2(0-1) (see Fig. 3). As a consequence, the statistical errors of the $I_{\rm EBL}$ estimates are two to three times as large as those for line 2. The best estimates obtained using the GAIA RVS and the Bright_rim fitting templates are are 0.82 ± 1.51 and −0.30 ± 2.35 cgs, respectively. Within their large error bars the estimates do not disagree with the results from line 2. Because of the substantially smaller errors and the good agreement between the GAIA RVS and the Bright_rim based values, we rank the line 2 results as superior to those obtained from line 3.

As our final result for the EBL intensity we adopt the value obtained for line 2: $I_{\rm EBL}(\lambda) = 1.62 \pm 0.76(\sigma_{\rm stat})$ 10^{-9} erg cm^{-2} s^{-1} Å^{-1} sterad^{-1}. This corresponds to $\lambda\, I_{\rm EBL}(\lambda) = 13.83 \pm 6.49(\sigma_{\rm stat})$ nW m^{-2} sterad^{-1}. In Fig. 6 we show this result together with a number of other $\lambda\, I_{\rm EBL}(\lambda)$ values in the visible and NIR from recent literature.

5. Discussion

A direct approach to EBL measurement is to observe the total dark night sky brightness and to model or make dedicated observations of all foreground components. For a ground-based observer they include the airglow, the zodiacal light, the (unresolved) starlight and the diffuse galactic light (DGL, light scattered by dust). The problem is further complicated because light has to pass through the atmosphere before reaching the telescope: each brightness component not only suffers extinction, but is also scattered by the molecular and aerosol components, each with its own scattering function (see Ashburn 1954; Mattila 2003; Bernstein et al. 2005).

5.1. EBL measurement with the dark cloud shadow method: Tentative detection at 8542 Å

Our observing method in the present paper is a differential one: the telescope is switched in rapid succession between an *on* position in the dark core of DC303.8-14.2 and an *off* position outside the cloud. The method is based on measurement of the *on–off* surface brightness difference spectrum between nearby positions on the sky. Our *on* and *off* positions are at slightly different ecliptic latitudes. Because the Ca II triplet lines are strong in the solar spectrum, this could cause a small systematic offset in their strengths in the *on–off* spectrum. Similarly, they are at slightly different zenith distances, and thus the airglow's zenith distance dependence could have an effect. However, the spatial separation between *on* and *off* is only 300″ (see Section 2.1), small enough so that the effect caused by these spatial gradients is of no importance. In this respect the dark cloud shadow method is equivalent to a night sky measurement carried out from a location outside the atmosphere, the zodiacal cloud, and even beyond any uniform surface-brightness layer, such as an interstellar dust sheet between us and the globule. The foreground components, 10–100 times brighter than the EBL, cause a substantial photon noise. In addition, as we discuss in Section 2, a substantial statistical uncertainty may be caused by the rapid time variability of the airglow.

The main challenge for the dark cloud method is the separation of the light scattered by dust particles in the cloud. To suppress its level the cloud core should have a high opacity. Although DC303.8-14.2 has a very substantial opacity, $\tau(8500) \gtrsim 10$, the scattered light still dominates over the EBL intensity by a factor of 10 or more.

In addition to the scattered light there is another diffuse surface brightness component ascribed to interstellar dust particles, the extended red emission (ERE) (Witt & Lai 2020). It has a continuous spectrum, covering parts or the whole wavelength range of ~5000–8000 Å. Its presence in the general diffuse medium was detected by Gordon et al. (1998) and has been recently confirmed by Chellew et al. (2022). An indication of its presence in DC303.8-14.2, and the nearby TPN globule was also detected Lehtinen & Mattila (2013); however, its presence in DC303.8-14.2 was limited to $\lambda < 8000$ Å. The Ca II triplet lines at 8500–8660 Å are thus beyond the ERE wavelength range.

The Ca II triplet lines offer a very good indicator for and a robust measure of the scattered starlight and its intensity. The depths of the lines in the globule's spectrum can be well fitted with a model spectrum of the incident starlight. The noise of the observed *on–off* FORS spectra determines the level of the statistical error of the resulting $I_{\rm EBL}$. The noise includes both the photon statistics and the effect of the AGL short-term time variation. The transfer of a FORS spectrum's noise to the statistical error of $I_{\rm EBL}$ is governed by the least-squares fitting procedure MPFITFUN. The rms noise for each spectrum and the resulting $\sigma_{\rm stat}$ value for $I_{\rm EBL}$ are given in Tables 3 and 4 for the individual spectral slots surrounding lines 1, 2, and 3, and for the whole spectral range 8470–8710 Å.

A systematic uncertainty of $I_{\rm EBL}$ is caused because the calibration of an extended surface brightness is different from that for a point source, such as a star. This is due to the aperture correction, $T(A)$. $T(A) = 1$ for a uniform extended surface brightness, such as the EBL or the widely distributed scattered light in the globule area. For observations of stars, $T(A)$ can be substantially smaller than 1, however; its uncertainty for our standard star observations with FORS2 introduces a ±8% systematic uncertainty to $I_{\rm EBL}$ (see Appendix D). Another systematic error is caused by the uncertainty of the attenuation factor, h_τ or $h_{\rm eff}$. It has been estimated to be ±2% for each of the two cases: with either GAIA_RVS or the observed Bright_rim spectrum used as template to fit the Dark_core spectrum (see Appendix C). The total absolute uncertainty (scaling factor) is thus estimated to be ±10%.

5.2. Other measurements of the EBL: Recent results and outlook

The EBL results from the CIBER rocket experiment (Matsuura et al. 2017) cover the wavelength range of our present study well. Their nominal EBL value at 8600 Å is given as $\lambda\, I_{\rm EBL}(\lambda) = 23.1 \pm 3.2(\sigma_{\rm stat}) + 15.1/-14.4\ (\sigma_{\rm syst})$ nW m^{-2} sterad^{-1} (their Table 3). It is, within their and our error estimates, consistent with our EBL value at 8542 Å. Recently, dark night sky measurements have been made with the LORRI experiment aboard NASA's New Horizons mission from locations in the outer Solar System, out to 57 AU. Two teams (Symons et al. 2023; Postman et al. 2024) have made use of the instrument's capabilities to measure the EBL intensity. Their most recent results are displayed in Fig. 6.

Our $I_{\rm EBL}$ value seemingly falls halfway between these two LORRI-based values. The comparison is problematic, however, since the LORRI band pass covers the very broad wavelength range of 4400–8700 Å and our narrow-band measurement falls at the very red end of LORRI's pass band where its response is low. Thus, even a substantially smaller or larger narrow band value of $I_{\rm EBL}$ at 8600 Å would have only a minor effect on LORRI's broad-band $I_{\rm EBL}$ value. Our $I_{\rm EBL}$ value is compatible, within its error limits, with the integrated galaxy light (IGL) estimate of Tompkins et al. (2026) without any contribution by an additional diffuse EBL component. On the other hand, our result is, within its error bars, consistent with a substantially larger $I_{\rm EBL}$ value, in agreement with the (Matsuura et al. 2017) results. These two independent results might indicate an upturn of the EBL intensity in the red/near-IR domain at $\lambda \gtrsim 7500$ Å. Such an upturn, if steep enough, would remain undetectable in the broad-band LORRI result.

Recently, O'Brien et al. (2025) using extensive 0.4–1.6 μm HST SKYSURF data, presented a new zodiacal light model. Based on this model, they announced the detection of an excess of diffuse light of 0.013 ± 0.006 MJy sterad^{-1} or ~45 nW m^{-2} sterad^{-1}, which they suggested most likely originates from a spherical inner Solar System zodiacal dust cloud. If instead it were of extragalactic origin, it would strongly exceed the upper bounds set by the broad-band LORRI mesurements and also our narrow-band EBL value at 8542 Å.

The diffuse Galactic light was the most important astrophysical foreground component in LORRI's fields that had to be analysed and subtracted. In that respect the situation is similar to the dark cloud method where the scattered light from dust represented the main task of our analysis. In principle, the dark cloud shadow method has the advantage that it is capable of narrow-band and even of spectroscopic measurements. However, the integrated starlight spectrum does not possess many other spectral features as good as the Ca II triplet lines that could be utilised for the scattered-light subtraction.

At present, improved observational techniques could already be realised via the dark cloud shadow method. These include the following: (1) a search for better (i.e. darker) target globules using the very deep low surface brightness surveys becoming available (the best targets would be those in the outskirts or

even outside our Galaxy; see Park & Kim 1998); (2) larger telescopes to enable a better spectral resolution, crucial for utilising deep absorption lines such as the Ca II triplet lines, which offer a very good indicator for and a robust measure of the scattered starlight and its intensity. The depths of the lines in the globule's spectrum can be well fitted with a model spectrum of the incident starlight. The noise of the observed *on–off* FORS spectra determines the level of the statistical error of the resulting $I_{\rm EBL}$. The noise includes both the photon statistics as well as the effect of the AGL short-term time variation. The transfer of a FORS spectrum's noise to the statistical error of $I_{\rm EBL}$ is governed by the least-squares fitting procedure MPFITFUN. The rms noise for each spectrum and the resulting $\sigma_{\rm stat}$ value for $I_{\rm EBL}$ are given in Tables 3 and 4 for the individual spectral slots surrounding lines 1, 2, and 3, and for the whole spectral range 8470–8710 Å.

A systematic uncertainty of $I_{\rm EBL}$ is caused because the calibration of an extended surface brightness is different from that for a point source, such as a star. This is due to the aperture correction, $T(A)$. $T(A) = 1$ for a uniform extended surface brightness, such as the EBL or the widely distributed scattered light in the globule area. For observations of stars, $T(A)$ can be substantially smaller than 1; however, its uncertainty for our standard star observations with FORS2 introduces a ±8% systematic uncertainty to $I_{\rm EBL}$ (see Appendix D). Another systematic error is caused by the uncertainty of the attenuation factor, h_τ or $h_{\rm eff}$. It has been estimated to be ±2% for each of the two cases: with either GAIA_RVS or the observed Bright_rim spectrum used as template to fit the Core-up spectrum (see Appendix D). The total absolute uncertainty (scaling factor) is thus estimated to be ±10%.

6. Conclusions

Our EBL measurement at 8542 Å, $\lambda I_{\rm EBL}(\lambda) = 13.8 \pm 6.5(\sigma_{\rm stat})\,{\rm nW\,m^{-2}\,sterad^{-1}}$ represents a tentative detection at the 2σ level. The systematic error is estimated to be ±10%. This value, while compatible with the integrated galaxy light (IGL) in the z band (Tompkins et al. 2026), still allows a contribution by unresolved sources or diffuse light of unknown origin to the EBL. Because it is essentially monochromatic, our $I_{\rm EBL}$ value is complementary to the recent New Horizons/LORRI (Symons et al. 2023; Postman et al. 2024) and blazar gamma-ray attenuation (Gréaux et al. 2024) $I_{\rm EBL}$ values, which were based on broad-band measurements in the range ~4400–8700 Å.

Acknowledgements. This research has made use of the following resources: data products from observations made with ESO Telescopes at the La Silla or Paranal Observatories under ESO programmes ID 099.A-0028, 0102.A-0280 and 0104.A-0192; FORS pipeline for data reduction and quality control of the FORS instrument data, as described in VLT-MAN-ESO-19500-4106; NASA's Astrophysics Data System Bibliographic Services; the European Space Agency (ESA) space mission Gaia. Gaia data are being processed by the Gaia Data Processing and Analysis Consortium (DPAC). Funding for the DPAC is provided by national institutions, in particular the institutions participating in the Gaia MultiLateral Agreement (MLA). The Gaia mission website is https://www.cosmos.esa.int/gaia. The Gaia archive website is https://archives.esac.esa.int/gaia; IRAF is distributed by the National Optical Astronomy Observatories, which are operated by the Association of Universities for Research in Astronomy, Inc., under cooperative agreement with the National Science Foundation.

References

Appenzeller, I., Fricke, K., Fürtig, W., et al. 1998, Messenger, 94, 1
Ashburn, E. V. 1954, J. Geophys. Res., 59, 67
Bernstein, R. A. 2007, ApJ, 666, 663
Bernstein, R. A., Freedman, W. L., & Madore, B. F. 2005, ApJ, 632, 713
Bruzual, G., & Charlot, S. 2003, MNRAS, 344, 1000
Carnall, A. C. 2017, arXiv e-prints [arXiv:1705.05165]
Chellew, B., Brandt, T. D., Hensley, B. S., Draine, B. T., & Matthaey, E. 2022, ApJ, 932, 112
Driver, S. P., Andrews, S. K., Davies, L. J., et al. 2016, ApJ, 827, 108
Fermi-LAT Collaboration (Abdollahi, S., et al.) 2018, Science, 362, 1031
Fitzgerald, M. P., Stephens, T. C., & Witt, A. N. 1976, ApJ, 208, 709
Flynn, C., Holmberg, J., Portinari, L., Fuchs, B., & Jahreiß, H. 2006, MNRAS, 372, 1149
Freyberg, M. J., Breitschwerdt, D., & Alves, J. 2004, Mem. Soc. Astron. It., 75, 509
Gordon, K. D. 2004, ASP Conf. Ser., 309, 77
Gordon, K. D., Witt, A. N., & Friedmann, B. C. 1998, ApJ, 498, 522
Gréaux, L., Biteau, J., & Nievas Rosillo, M. 2024, ApJ, 975, L18
Hartley, M., Manchester, R. N., Smith, R. M., Tritton, S. B., & Goss, W. M. 1986, A&AS, 63, 27
Hauser, M. G., Arendt, R. G., Kelsall, T., et al. 1998, ApJ, 508, 25
Henyey, L. G., & Greenstein, J. L. 1941, ApJ, 93, 70
Kainulainen, J., Lehtinen, K., Väisänen, P., Bronfman, L., & Knude, J. 2007, A&A, 463, 1029
Korngut, P. M., Kim, M. G., Arai, T., et al. 2022, ApJ, 926, 133
Koushan, S., Driver, S. P., Bellstedt, S., et al. 2021, MNRAS, 503, 2033
Lauer, T. R., Postman, M., Weaver, H. A., et al. 2021, ApJ, 906, 77
Lauer, T. R., Postman, M., Spencer, J. R., et al. 2022, ApJ, 927, L8
Le Borgne, J. F., Bruzual, G., Pelló, R., et al. 2003, A&A, 402, 433
Lehtinen, K., & Mattila, K. 2013, A&A, 549, A91
Matsuura, S., Arai, T., Bock, J. J., et al. 2017, ApJ, 839, 7
Mattila, K. 1970, A&A, 9, 53
Mattila, K. 1976, A&A, 47, 77
Mattila, K. 2003, ApJ, 591, 119
Mattila, K., Lehtinen, K., Väisänen, P., von Appen-Schnur, G., & Leinert, C. 2017a, MNRAS, 470, 2133
Mattila, K., Väisänen, P., Lehtinen, K., von Appen-Schnur, G., & Leinert, C. 2017b, MNRAS, 470, 2152
Mattila, K., Haas, M., Haikala, L. K., et al. 2018, A&A, 617, A42
O'Brien, R., Arendt, R. G., Windhorst, R. A., et al. 2025, arXiv e-prints [arXiv:2510.18231]
Park, C., & Kim, J. 1998, ApJ, 501, 23
Postman, M., Lauer, T. R., Parker, J. W., et al. 2024, ApJ, 972, 95
Sandqvist, A. 1977, A&A, 57, 467
Symons, T., Zemcov, M., Cooray, A., Lisse, C., & Poppe, A. R. 2023, ApJ, 945, 45
Togi, A., Witt, A. N., & John, D. S. 2017, A&A, 605, A99
Tompkins, S. A., Driver, S. P., Robotham, A. S. G., et al. 2026, MNRAS, accepted [arXiv:2507.03412]
Wainscoat, R. J., Cohen, M., Volk, K., Walker, H. J., & Schwartz, D. E. 1992, ApJS, 83, 111
Witt, A. N., & Lai, T. S. Y. 2020, Ap&SS, 365, 58
Witt, A. N., & Stephens, T. C. 1974, AJ, 79, 948
Witt, A. N., Oliveri, M. V., & Schild, R. E. 1990, AJ, 99, 888
Yeung, M. C. H., Freyberg, M. J., Ponti, G., et al. 2023, A&A, 676, A3
Zemcov, M., Immel, P., Nguyen, C., & e. a., 2017, Nat. Commun., 8, 15003

Appendix A: Observations and data reduction

The observations were conducted in years 2017, 2019, 2020, and 2021. Of the 27 spectroscopic observing blocks 21 were observed between airmasses 1.65 to 1.74 and only three blocks were observed at airmasses 1.83 to 1.94. The minimum airmass reached for DC303 (Decl. = −77°) at Paranal is 1.65. The number of observed blocks in months each year are listed in Table A.1.

Table A.1. Number of observing blocks observed each year and month.

Year	Jan.	Feb.	Mar.	Jun.	Jul.
2017		4[a]		4	
2019	1		5		
2020		1	9		
2021	1		4		2

[(a)]Pre-imaging

A.1. Airglow

A representative of our darkest total sky surface brightness spectra of the Ca II triplet wavelength region; the spectrum was obtained on March 3rd 2020 at an elevation of 37° (airmass 1.65), is shown in Fig. A.1. The dominating component is the AGL. For comparison, the ZL+DGL contribution is ≤50 cgs (see O'Brien et al. 2025), that is ≤20% of the minimum sky brightness over this spectral range.

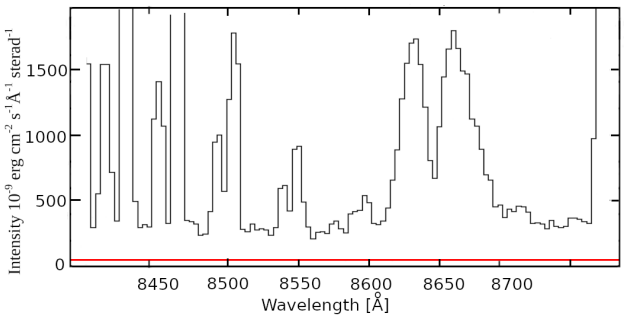

Fig. A.1. Surface brightness in the A_100″-off position in one observing block obtained on March 3, 2020, at an elevation of 37°. The level of expected zodiacal light surface brightness (approximately 50 cgs) is indicated with a red line.

A.2. Reduced on–off spectra

The reduced extracted *on–off* spectra in the slit sections listed in Table 2 are shown in Fig. A.2. Blue and red are used to distinguish the spectra for the sub-sets of 179 and 228 spectra, selected for minimum-AGL residuals, respectively.

Appendix B: The convolved GAIA RVS starlight spectrum

FORS instrumental profile (channel width 0.82 Å), constructed using the FORS wavelength calibration lamp spectra, was resampled to correspond to the GAIA spectrum channel width of

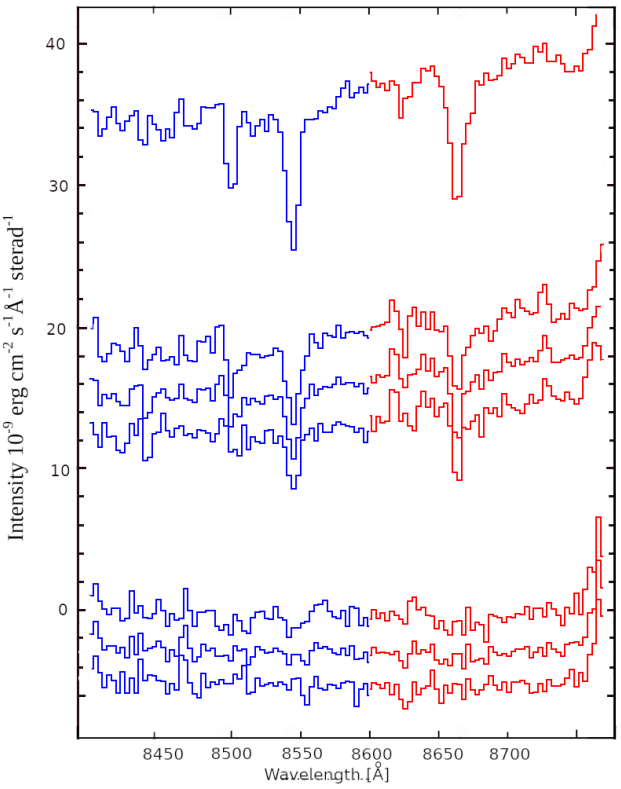

Fig. A.2. Final reduced spectra in the slit sections discussed in this paper: (from top to bottom) Bright_rim, Core-up, Core-100″, Core-low, A_low-off, A_100″-off, A_core-off. The spectra for the sub-sets of 179 and 228 individual spectra, selected for minimum-AGL residuals, are shown as blue and red for $\lambda < 8600$ Å and $\lambda > 8600$ Å, respectively.

0.1 Å. This profile was used to convolve the normalised GAIA RVS sum spectrum (Section 3.2.1) and then resampled using SpecRess (Carnall 2017) to the same channel width as the FORS spectra to be fitted. The original GAIA high resolution spectrum for $g = 0.75$, the convolved GAIA spectrum, and the GAIA spectrum resampled to the FORS binned 3.28 Å channel width are shown in the upper part of Fig. B.1 in black, blue, and red, respectively. In the lower part this resampled GAIA spectrum together with the resampled GAIA spectrum assuming $g = 0.50$ are shown.

Appendix C: EBL shadowing by the globule, attenuation factor $h(\tau)$

As has already been discussed in Section 3.1 the globule not only attenuates the line-of-sight EBL but also scatters the photons of the isotropic EBL into the observer's direction. The surface brightness difference, globule *(on)* minus transparent surroundings *(off)*, is given by Eq. (1):
$\Delta I_{\rm obs}(\lambda) = \Delta I_{\rm sca}(\lambda) - I_{\rm EBL} h(\tau)$
where we introduced the notation $h(\tau) = 1 - e^{-\tau} - f_{\rm sca}(\tau)$, to be called the attenuation factor.

The surface brightness difference *on–off* is almost completely accounted to starlight which has been scattered by dust in the globule. This component, $\Delta I_{\rm sca}(\lambda)$, when expressed as fraction of the infalling illumination by starlight over the sky, can be used to estimate the scattered fraction, $f_{\rm sca}(\tau)$, of the EBL. In doing so we have to take into account that, while the EBL is isotropic, the distribution of the ISL is concentrated towards

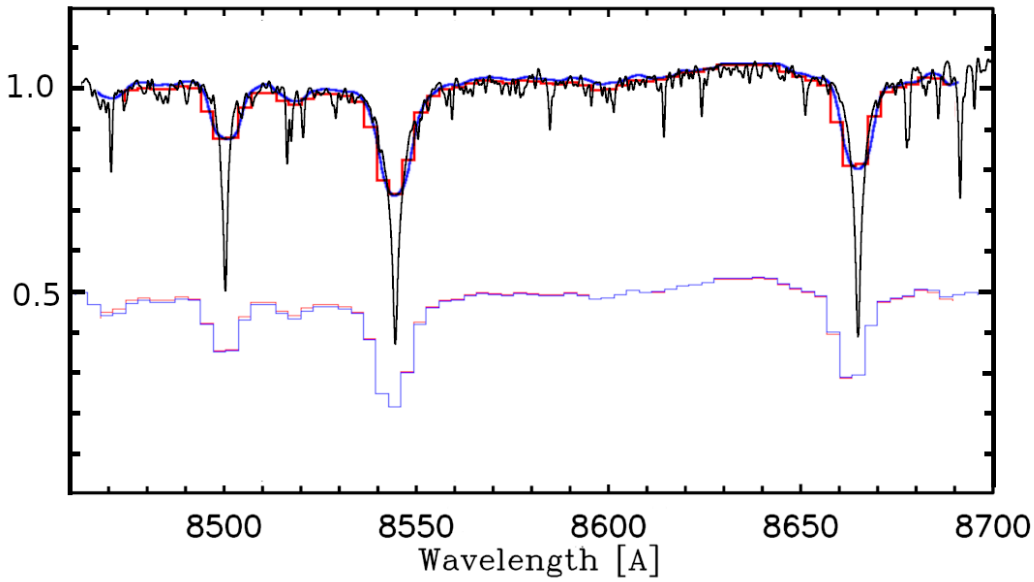

Fig. B.1. Top: Summed normalised GAIA surface brightness assuming scattering function with asymmetry parameter g = 0.75 (Section C) (black), convolved using the FORS instrumental profile (blue), and resampled to the resolution of 3.28 Å (red). Bottom: GAIA spectra smoothed using FORS instrumental profile and resampled to the resolution of 3.28 Å assuming asymmetry parameter g = 0.75 (red), and 0.50 (blue) offset by -0.5 units.

the Galactic plane. To estimate the infalling starlight at $\lambda \sim 8600$ Å, effective for the illumination of the globule, we make use of the Pioneer all-sky map at the R_p band (Gordon et al. 1998) and the web page [3]. The average ISL surface brightness with equal weights all over the sky is $\langle I_{\rm ISL}(R_p)\rangle$ = 151 10^{-9}erg cm^{-2}s^{-1}Å^{-1}sterad^{-1}; this estimate includes also the bright stars, $m < 6.5$ mag (Section 3.1.1 and Table 5, Mattila et al. 2018). It corresponds to the case where the dust would be isotropically scattering. However, the dust has a strongly forward-directed scattering function as discussed in Section 3.2.1 above. For a Henyey-Greenstein scattering function with an asymmetry parameter $g = \langle\cos\Theta\rangle = 0.75$ the weighted mean ISL sky brightness as seen by the globule is $\langle I_{\rm ISL}(R_p)\rangle$ = 253 10^{-9}erg cm^{-2}s^{-1}Å^{-1}sterad^{-1} .

In order to refer these R_p band values, with a pivot wavelength of 6441 Å, to λ = 8600 Å we make use of the Lehtinen & Mattila (2013) Milky Way SED model. It gives the scaling factor $I_{\rm ISL}(8600)/I_{\rm ISL}(R_p) = 0.88$. Then, the effective sky brightness weighted according to $g = 0.75$, is $\langle I_{\rm ISL}(8600)\rangle$ = 223 10^{-9}erg cm^{-2}s^{-1}Å^{-1}sterad^{-1} . If weighted according to $g = 0.50$, the effective sky brightness would be $\langle I_{\rm ISL}(8600)\rangle$ = 192 10^{-9}erg cm^{-2}s^{-1}Å^{-1}sterad^{-1} .

The optical depth through the core of DC303.8-14.2 is > 10; thus, the transmission $e^{-\tau}$ is negligible. For the bright rim the optical depth can be estimated via two methods: first, via direct JHK_s photometry (Kainulainen et al. 2007) and secondly, via the observation that the maximum surface brightness of scattered light in globules and dark nebula cores occurs at an optical depth of $\sim 1.5-2.5$ (Witt & Stephens 1974; Mattila et al. 2018). We adopt $\tau(8600) = 2$.

With reference to the results for line 2 (8542 Å) in Tables 3 and 4 we adopt for $h(\tau)I_{\rm EBL}$ the values 1.5 and 1.1 10^{-9}erg cm^{-2}s^{-1}Å^{-1}sterad^{-1} for the Core-up and Bright_rim, respectively. The $\Delta I_{\rm sca}(8600)$ values are then estimated to be 14.5 – 20.8 and 37.7 10^{-9}erg cm^{-2}s^{-1}Å^{-1}sterad^{-1} for the the three core sections and the Bright_rim, respectively. These values result in the ratios $\Delta I_{\rm sca}/\langle I_{\rm ISL}\rangle = f_{\rm sca}(\tau)$ = 0.065 – 0.093 and 0.17. for the core sections and the Bright_rim, respectively.

With these estimates we end up with value $h(\tau) = 0.92$ as the best estimate to be used for the three core positions; it is the mean of the values for Core-up and Core-low and it coincides with the value for Core-100″ . The value $h(\tau) = 0.69$ is obtained for the Bright_rim (see Table C.1). With an estimated error of ±10% for both $\Delta I_{\rm sca}$ and $\langle I_{\rm ISL}\rangle$ we estimate the systematic error to be ±2% and ±4% for the Core-up and Bright_rim, respectively. However, for the case when the bright rim is used as a template to fit the dark core spectrum (see Section 3.2.2), $h_{\rm eff}$ = 0.58 with an error of ±2%, as well. If $g = 0.50$ had been adopted insted of $g = 0.75$ the attenuation factors of 0.91, 0.66 and 0.58 would have resulted, instead. The differences relative to the case $g = 0.75$ are small and cause no changes to our EBL values or their error estimates.

Appendix D: Aperture correction

The intensity (surface brightness) of an extended source in 10^{-9}erg cm^{-2}s^{-1}Å^{-1}sterad^{-1} is given by

$$I(\lambda) = \frac{S(\lambda)T(A)}{\Omega}C(\lambda), \qquad \text{(D.1)}$$

where $C(\lambda)$ is the signal in instrumental units (ADU), Ω the solid angle of the aperture in steradians, and $S(\lambda)$ the sensitivity function in units of 10^{-9} erg cm^{-2}s^{-1}Å^{-1}/ADU, as determined from the standard-star observations. $T(A)$ is the aperture correction, which is required when calibrating an extended surface brightness with standard star observations. In the measurement of a

[3] https://www.stsci.edu/~kgordon/pioneer_ipp/Pioneer_10_11_IPP.html

Table C.1. Empirical determination of the attenuation factor at $h(\tau) = 1 - e^{-\tau} - f_{\rm sca}(\tau)$ at 8600 Å using scattered starlight from DC303.8-14.2.

	Core-up [cgs]	Core-low [cgs]	Core-100″ [cgs]	Bright_rim [cgs]
$\Delta I_{\rm obs}$	19.3	13.0	16.5	36.6
$I_{\rm EBL}h(\tau)^{a,b}$	1.5	1.5	1.5	1.1
$\Delta I_{\rm sca}$	20.8	14.5	18.0	37.7
$\langle I_{\rm ISL}\rangle^{c}$	223	223	223	223
$\Delta I_{\rm sca}/\langle I_{\rm ISL}\rangle = f_{\rm sca}(\tau)$	0.093	0.065	0.081	0.17
$\tau(8600)$	> 10	> 10	> 10	~2
$e^{-\tau}$	0	0	0	~14
$h(\tau)$	0.907	0.935	0.919	0.69

[(a)] $I_{\rm EBL}h(\tau)$ is used here as a correction term to be added to $\Delta I_{\rm obs}$; different values of $h(\tau)$ have been iteratively used.
[(b)] The value adopted for $I_{\rm EBL}$ is 1.62 10^{-9}erg cm^{-2}s^{-1}Å^{-1}sterad^{-1}.
[(c)] The effective sky brightness at λ = 8600 Å.

uniform extended source the flux that is lost from the solid angle Ω, as defined by the focal plane aperture, is compensated by the flux that is scattered and diffracted into the aperture from the sky outside of the solid angle Ω; thus $T(A) = 1$. However, for the standard stars used to calibrate the surface brightness in physical flux units the aperture correction, to be noted by $T(A)^*$, is < 1. Only the fraction $T(A)^*$ of the flux from the star is contained within the aperture, while the fraction $1 - T(A)^*$ is lost outside the aperture by diffraction and scattering in the telescope and instrument optics.

D.1. Aperture correction for standard stars

Spectrophotometric standard stars were observed in the ESO calibration service program using a 5″ slit. The spectra were extracted from the sum of stellar flux in the extraction window of 3.0″ width in the spatial direction. In order to estimate the flux fraction falling outside of the extraction window we used the stacked spectrum of nine standard star observations available for our program. The flux fraction up to a distance of 20″ was found to be 0.172 with an estimated error of ±0.02 The wavelength range covered was 8300 - 8800 Å. This estimate can be compared with the results presented in Mattila et al. (2017a), sect. 6.4. They also used FORS2 at UT1 and a similar spectrometer set-up. The wavelength range covered three slots, 3500–4250, 4250–5000, and 5000–6000 Å. From a stacked spectrum of 17 standard stars they estimated the energy falling outside of the 2.5″ × 5″ extraction slot, up to a distance of 20″. No wavelength dependence was found, and the mean value for these three slots was $1 - T(A)^* = 0.143 \pm 0.006$, which is within the errors consistent with our present result for 8300 - 8800 Å

The fraction of energy falling outside of 20″ was estimated by Mattila et al. (2017a) using measurements (FORS1 at UT2) of Sirius' aureole: $1 - T(A)^*$ was found to be 0.029 for the flux fraction between 20″– 100″, and 0.038 between 100″– 2° ; the values were closely the same in blue and visual. With an estimated uncertainty of ±50% for each of these estimates the total error was estimated to be ~ ±0.05. In spite of the wavelength difference we adopt this value for our present wavelength slot as well.

Summing up, at 8300 - 8800 Å the total fraction of the standard stars' flux lost between 3″ and 2° is estimated to be $1 - T(A)^* = 0.24 \pm 0.06$ and thus, the aperture correction is $T(A)^* = 0.76 \pm 0.06$. Because of the aperture correction the standard star fluxes to be used for the calibration of the surface brightnesses are, instead of their list values I_λ, given by $T(A)^* I_\lambda$. As a consequence, the surface brightness measurements, scaled by the standard star list values, have to be re-scaled down by the factor $T(A)^*$.

Appendix E: Synthetic ISL spectrum model for 8450 - 8700 Å

As has been described in Section 3.2.1 a major part of the ISL intensity at 8500 - 8700 Å is covered by the sum of RVS spectra available in the GAIA DR3 for stars brighter than 12 mag. In this appendix we shall investigate to what extent the contribution by the fainter stars with $G_{RVS} > 12$ mag influences the Ca II triplet spectrum at 8500 - 8700 Å.

For modelling of the ISL spectrum we make use of the spectral synthesis method which has commonly been used to analyse the contributions by different stellar populations to the total light of an external galaxy or star cluster (see e.g. Bruzual & Charlot 2003). Here, we have addressed the opposite problem: given the number densities and the spatial distributions of the different spectral types of stars in the Solar neighbourhood, what is the spectrum of their integrated light (ISL) for different magnitude intervals and in different directions over the sky. Our results for the ISL spectrum at 8450 - 8700 Å make use of the spectral synthesis modelling as presented in Mattila et al. (2017b).

There, a simple model of the Galactic structure was adopted in which stars and dust are distributed in plane parallel layers. Stars were divided into 72 spectral groups covering the different parts of the HR-diagram. The division was made according to the approach of Flynn et al. (2006) based on their analysis of the *Hipparcos* database. The spectral groups were compiled under the following seven categories: *(i, ii)* main sequence (thin and thick disk), *(iii, iv)* clump stars (thin and thick disk), *(v, vi)* old giants (thin and thick disk), *(vii)* young giants. Each group was characterised by the following parameters: the mean absolute magnitude M_V; the number density $D(0)$ and the stellar emission coefficient $j_i(0)$ in the Galactic plane, $z = 0$; and the scale height h_z for a distribution of the form $D(z) = D(0)\mathrm{sech}(z/h_z)$. Because of the limited distance range of *Hipparcos*, its coverage for the supergiants was sparse. This group was, therefore, complemented by using the compilation of Wainscoat et al. (1992).

For the synthetic model of the ISL spectrum a spectral library is needed with good coverage of spectral types and luminosity classes as well as a sufficient spectral resolution, corresponding to or better than that of the observed spectra. The STELIB

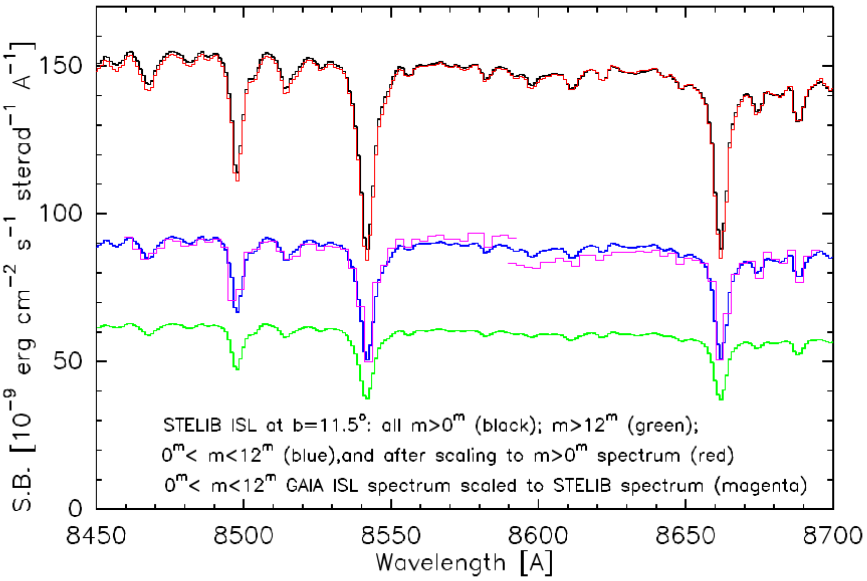

Fig. E.1. Synthetic ISL spectra based on the STELIB spectral library. The spectra are shown for different magnitude intervals: total starlight $m > 0$ mag (black); $m > 12$ mag (blue); $0 < m < 12$ mag (green). In order to demonstrate the agreement between the total ISL and the $0 < m < 12$ mag spectra, a scaled version of the latter (in red) is overplotted on the total spectrum. A suitably re-scaled GAIA/RVS spectrum is shown as the magenta line overplotted upon the model spectrum for $0 < m < 12$ mag (blue line). Because of the difference in baseline slopes, the GAIA/RVS spectrum has been cut at 8590 Å and is shown as two pieces.

library (Le Borgne et al. 2003), with its spectral resolution of $\lesssim 3$ Å (FWHM), matches well the resolution requirement for our VLT/FORS2 spectra. From this library the best template stars for each stellar group were chosen: besides the spectral class and absolute magnitude M_V, also the colour indices $B-V$ and $V-I_c$ were used as selection criteria.

ISL model spectra covering the Ca II triplet wavelength region are shown in Fig. E.1. The spectra are for the galactic latitude $|b| = 11.5°$. No galactic longitude dependence is included in the model, and symmetry is assumed w.r.t. the galactic plane. The adopted galactic latitude corresponds to a weighted mean of contributions from Milky Way areas around the direction of the DC303.8-14.2 . The spectra are shown for three different magnitude intervals, $m > 0$ (black), $0 < m \leq 12$ mag (blue) and $m > 12$ mag (green). The relative intensity levels are seen to correspond to the starcount results, presented in Section 3.2.1: approximately 40% of the total ISL is contributed by stars with $m > 12$ mag. In order to see whether the missing stars have a strong effect on the Ca II triplet lines we have overplotted the spectrum for $0 < m < 12$ mag, suitably scaled (red line), upon the total ISL spectrum. The good agreement between the black and red lines demonstrates that the spectrum for $0 < m \leq 12$ mag is a good representative also for the total ISL.

Being based on the STELIB library, the model spectra shown in Fig. E.1 have a resolution of $\lesssim 3$ Å (FWHM) and have been plotted with a step size of 1 Å corresponding to the original database. In order to enable comparison with STELIB, we have smoothed the GAIA RVS spectrum to a resolution of 2.7 Å . Suitably re-scaled, it has been overplotted in Fig. E.1 as the magenta line on the model spectrum for $0 < m \leq 12$ mag (blue line). A good agreement is demonstrated between the GAIA RVS and the STELIB synthetic spectra.